Building Ruddlesden-Popper and Single Perovskite Nanocomposites: A New Strategy to Develop High-Performance Cathode for Protonic Ceramic Fuel Cells

Huangang Shi, Chao Su, Xiaomin Xu, Yangli Pan, Guangming Yang, Ran Ran, and Zongping Shao**

Dr. H. Shi

School of Environmental Engineering, Nanjing Institute of Technology, Nanjing, 211167, China

Dr. C. Su

School of Energy and Power, Jiangsu University of Science and Technology, Zhenjiang, 212100, China
E-mail: chao.su@just.edu.cn

Dr. H. Shi, Dr. C. Su, Dr. X. Xu, Y. Pan, Prof. Z. Shao

WA School of Mines, Minerals, Energy and Chemical Engineering (WASM-MECE), Curtin University, Perth, WA 6102, Australia
E-mail: zongping.shao@curtin.edu.au

Dr. G. Yang, Dr. R. Ran, Prof. Z. Shao
State Key Laboratory of Materials-Oriented Chemical Engineering, College of Chemical Engineering, Nanjing Tech University, Nanjing, 211816, China

Keywords: cathodes, nanocomposites, perovskites, protonic ceramic fuel cells, Ruddlesden-Popper

ABSTRACT: The development of a highly active and robust cathode is a key step to realize the practical application of protonic ceramic fuel cells (PCFCs). Here we unveil a new strategy to develop superior cathodes for PCFCs by the formation of Ruddlesden-Popper (RP)-single perovskite (SP) nanocomposites. We specifically design materials with the nominal compositions of $LaSr_xCo_{1.5}Fe_{1.5}O_{10-\delta}$ (LSCFx, x = 2.0, 2.5, 2.6, 2.7, 2.8, and 3.0). RP-SP nanocomposites (x = 2.5, 2.6, 2.7, and 2.8), SP oxide (x = 2.0), and RP oxide (x = 3.0) are obtained through a facile one-pot synthesis. A synergy is created between RP and SP in the nanocomposites, resulting in more favorable oxygen reduction activity compared to pure RP and SP oxides. More importantly, such synergy effectively enhances the proton-conductivity of nanocomposites, consequently significantly improving the cathodic performance of PCFCs. Specifically, the area-specific resistance of LSCF2.7 is only 40% of LSCF2.0 on $BaZr_{0.1}Ce_{0.7}Y_{0.2}O_{3-\delta}$ (BZCY172) electrolyte at 600 °C. Additionally, such synergy brings about a reduced thermal expansion coefficient of the nanocomposite, making it better compatible with BZCY172 electrolyte. Therefore, an anode-supported PCFC with LSCF2.7 cathode and thin-film BZCY172 electrolyte brings an attractive peak power output of 391 mW cm^{-2} and attractive durability at 600 °C.

1. Introduction

Solid oxide fuel cells (SOFCs) have been paid enormous importance from both scientific and industrial communities during the past two decades because of their numerous advantageous features as compared to polymer electrolyte membrane fuel cells, such as high electrode reaction kinetics allowing the use of precious metal-free electrode materials, simplified water management, fuel flexibility, and potential co-generation of power and chemical.[1-3] Typically, SOFCs are classified into two types according to the different conduction mechanism of the electrolytes, i.e. oxygen ion conducting SOFCs (O-SOFCs) and proton-conducting SOFCs, also known as protonic ceramic fuel cells (PCFCs). Nowadays, it is widely recognized that reducing operating temperatures of SOFCs to the

intermediate-to-low temperature (ILT) range (i.e. 400-700 °C) can dramatically stimulate the commercialization of this attractive technology, because such drop in operating temperature can effectively cut operating cost, prolong cell lifetime, and enable more flexible sealing.[4-6] The power output is an important parameter to determine the practical applicability of fuel cells. It is closely related to the polarization resistance of electrodes and the ohmic resistance of the electrolyte in fuel cells. Therefore, there are great efforts to maintain low values for both of them at reduced operating temperatures. Considering the ohmic resistance is in direct proportion to the electrolyte thickness and in opposite proportion to the conductivity of electrolyte, an anode-supported thin-film electrolyte cell configuration is widely adopted for ILT-SOFCs. Given that the relatively low activation energy of proton diffusion compared to oxygen-ion, in principle, PCFCs are more suitable than O-SOFCs for the operation at reduced temperatures.[7,8] Based on the theoretical conductivity of benchmark proton-conducting electrolytes, such as $BaZr_{0.1}Ce_{0.7}Y_{0.1}Yb_{0.1}O_{3-\delta}$ (BZCYYb), the ohmic resistance of a thin-film electrolyte with the thickness of ~10 μm is still affordable for operating at a temperature down to 450 °C.[9,10] In the past decade, tremendous efforts have been made in the fabrication of thin-film proton-conducting electrolytes and significant progress has been gained.[11-14] For example, spray casting, spin coating, screen printing, and sintering aid have turned out to be effective methods in preparing high-quality proton-conducting electrolytes with mass production capabilities. It suggests that the development of efficient electrode materials is of particular importance for realizing high power outputs of PCFCs at ILT range. Since the cathodic performance

decisively determines the electrode polarization resistance, the search for high-performance cathodes that performs well in ILT-PCFCs has attracted more and more attention.[15-20]

The cathodic reactions in PCFCs are more complicated than that in O-SOFCs. For typical cathodic processes in O-SOFCs, the oxygen is first adsorbed on the electrode surface, where it undergoes dissociation, diffusion, and charge transfer. If a mixed oxygen ion and electron conducting (MIEC) electrode is applied, the charge transfer can occur across the entire exposed electrode surface, and then the as-formed oxygen ion diffuses through the electrolyte to the anode side. Therefore, the development of MIEC cathodes is a general research trend for ILT O-SOFCs.[21,22] As to PCFCs, the cathodic processes involve the oxygen reduction reaction (ORR) and the production of water by O^{2-} reduced in the cathode and H^{+} transported from the anode. It implies that an excellent cathode of PCFCs should possess both high bulk proton conductivity and oxygen surface exchange kinetics, while oxygen ion conductivity is not as important as in O-SOFCs.[23] Since the perovskite-type proton conductors usually show low thermal expansion coefficient (TEC), the cathode materials should also have relatively low TEC to ensure their good thermomechanical compatibility.[24-26] Single perovskite (SP) oxides have been broadly applied as the electrodes for O-SOFCs. In particular, many cobalt-based perovskite oxides exhibit superb mixed oxygen ionic and electronic conductivity and oxygen surface exchange kinetics, thus guaranteeing that they are excellent cathodes materials for ILT O-SOFCs.[27-31] However, in general, the cobalt-based perovskite oxides have large TEC, and the rich cobalt in the perovskites may suppress proton conduction.[32,33] Consequently, the cobalt-based

perovskite oxides usually display insufficient activity for PCFCs.[34,35] The Ruddlesden-Popper (RP) perovskite oxides, which are layered structure with alternative perovskite layer and metal oxides, have received considerable attention in recent years. Compared to SP oxides, some RP oxides show higher proton conductivity, thus displaying promising performance as the cathodes of PCFCs.[36-38] However, in comparison to SP oxides, RP oxides generally show poorer oxygen surface exchange kinetics and lower electronic conductivity.[39,40]

Compared to single phase oxides, it has recently been found that many nanocomposites have better catalytic or electrocatalytic activity for various reactions, such as peroxymonosulfate activation for waste water remediation, ORR at elevated temperature, and oxygen evolution reaction (OER) in alkaline media at room temperature.[41-44] The strong interaction between the two phases in the nanocomposites could inhibit the thermal expansion of the materials. Additionally, the introduction of synergistic effect can alter the electronic structure of both phases, thereby optimizing the bulk diffusion and surface properties.[45,46] It indicates that the strongly interacting RP-SP nanocomposites may be potential cathodes for PCFCs. In the past, several nanocomposites have been successfully prepared through a one-pot synthesis using organic precursors.[47-50] However, it is a big challenge to precisely control the mass ratio of each phase in the nanocomposite. Very recently, we have developed a method of an A-site cation deficiency-promoted phase separation for preparing RP-SP nanocomposites with an accurately controlled mass ratio of two phases. The as-obtained nanocomposite showed a promising performance as the OER electrocatalyst.[51] It provides

a useful platform for studying the potential benefits of forming RP-SP nanocomposite to enhance the ORR performance in PCFCs.

Herein, several RP-SP nanocomposites, pure RP oxide, and pure SP oxide with the nominal compositions of $LaSr_xCo_{1.5}Fe_{1.5}O_{10-\delta}$ (LSCFx, x = 2.0, 2.5, 2.6, 2.7, 2.8, and 3.0) were prepared and explored as the cathodes for O-SOFCs and PCFCs for operating at ILT range. Compared to the single RP (LSCF3.0) and SP (LSCF2.0) perovskites, the as-obtained RP-SP nanocomposite with an appropriate mass ratio of RP and SP can effectively enhance the ORR activity of PCFC, which is attributed to the increased bulk proton conductivity and favorable oxygen surface exchange kinetics by building a strong interacted nanocomposite. It thus provides a new strategy for the development of alternative cathodes for PCFCs operation at ILT range.

2. Results and Discussion

2.1. Basic Properties of RP-SP Nanocomposites

As shown in Figure S1, all X-ray diffraction (XRD) peaks of LSCF2.0 and LSCF3.0 can be well indexed according to the SP with cubic lattice symmetry and the layered RP structure, respectively, while the other four samples can be indexed based on a mixture of RP and SP. According to Rietveld refinement of the XRD patterns, LSCFx samples (x = 2.5, 2.6, 2.7, and 2.8) were the mixtures of LSCF2.0 and LSCF3.0 with the mass ratios of 5:5, 4:6, 3:7, and 2:8, respectively.[51] Based on the half

width of the diffraction peaks at (111) plane for SP and (118) plane for RP, the average crystalline size of RP and SP phases in LSCF2.5, LSCF2.6, LSCF2.7, and LSCF2.8 are found to be 94/45 (RP/SP), 65/66. 45/45 and 57/55 nm, respectively. It suggests that RP and SP in these materials are both nanocrystallines, confirming the formation of nanocomposites, which agrees well with our previous studies.[51] High-resolution transmission electron microscopy (HRTEM) images of LSCF2.7 also confirm the formation of mixed phases of RP and SP (Figure S2).

To examine whether the RP-SP nanocomposites can present stably at the operating temperatures of IT-SOFCs, LSCF2.7 was selected as a representative nanocomposite to be further calcined at 600 °C in air for a prolonged period of 200 h. As shown in **Figure 1**a, the XRD pattern of LSCF2.7 after sintering for 200 h is almost the same as that of the fresh LSCF2.7, which can still be indexed well according to the mixture of RP and SP, indicating the high thermodynamic stability of the nanocomposite. The N_2 adsorption/desorption isotherms of LSCF2.7 before and after sintering at 600 °C for 200 h is shown in Figure 1b. Both curves are similar and can be assigned to type III, implying the pore-free nature of the materials. It suggests the specific surface area is mainly contributed from the exposed external surface of the particles. After calcination at 600 °C for 200 h, the specific surface area of LSCF2.7 only showed a slight decrease from the initial 2.03 to 1.84 $m^2 g^{-1}$, signifying the superior sintering resistance of the nanocomposites.

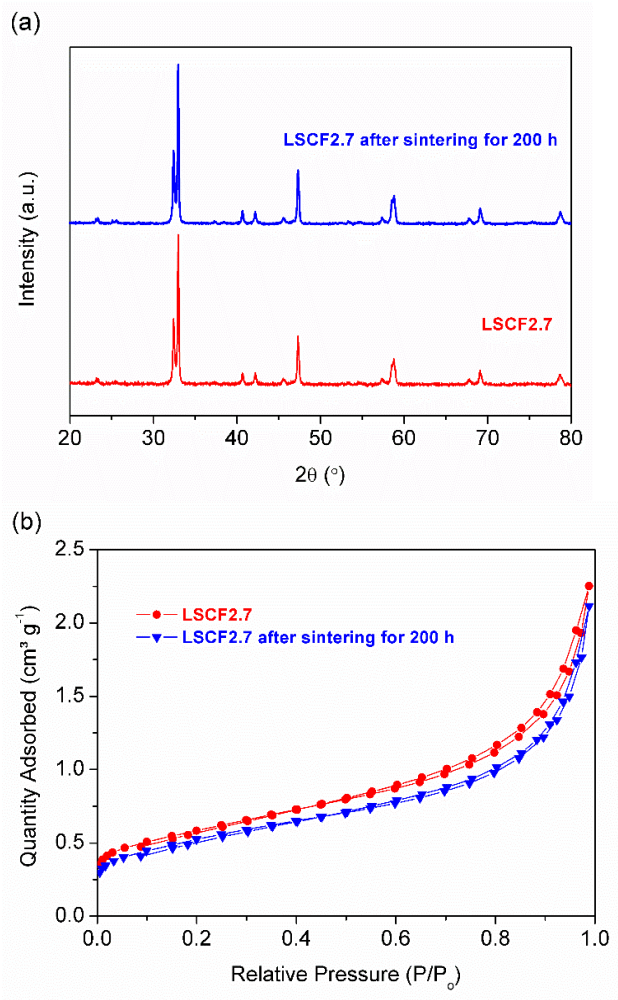

Figure 1. (a) XRD patterns and (b) N_2 adsorption/desorption isotherms of LSCF2.7 before and after calcining at 600 °C for 200 h.

In addition to chemical compatibility, thermomechanical compatibility between the electrolyte and the cathode is also a big concern for the stable operation of fuel cells. The TECs of

electrolyte materials, $Sm_{0.2}Ce_{0.8}O_{1.9}$ (SDC) and $BaZr_{0.1}Ce_{0.7}Y_{0.2}O_{3-\delta}$ (BZCY172), were reported to be 12.6 $\times 10^{-6}$ and 10.1 $\times$ 10^{-6} K^{-1}, respectively, within the temperature range of 400-700 °C.[52,53] Cobalt-based perovskite oxides usually show large TECs (20 $\times$ 10^{-6} - 30 $\times$ 10^{-6} K^{-1}), which can be attributed to the chemical expansion related to the easy change in oxidation state and spin state of cobalt ion.[54] Conversely, the RP oxides generally exhibit relatively low TECs. On the basis of the dilatometric curves (**Figure 2**a), the TECs are calculated to be 27.7, 26.4, and 24.6 $\times$ 10^{-6} K^{-1} for LSCF2.0, LSCF3.0, and LSCF2.7, respectively. As expected, LSCF2.7 showed the smallest TEC among the three samples. The low TEC thus makes LSCF2.7 more compatible with the electrolyte, which is beneficial for the fuel cell application. We previously demonstrated that the intimate interaction between the SP and double perovskite (DP) phases in nanodomain can effectively suppress the oxidation state change of transition metal elements in the oxides, thereby inhibiting chemical expansion.[46] The oxidation state transition capability of these three samples were then examined by an oxygen temperature-programmed desorption (O_2-TPD) technique. As shown in Figure 2b, LSCF2.7 has the lowest oxygen release degree, signifying that the transition in oxidation state of transition metal elements is significantly weakened by the formation of RP-SP nanocomposite. Furthermore, the onset temperature of oxygen release for LSCF2.7 is the lowest among the three samples, suggesting the highest mobility of the oxygen in LSCF2.7.

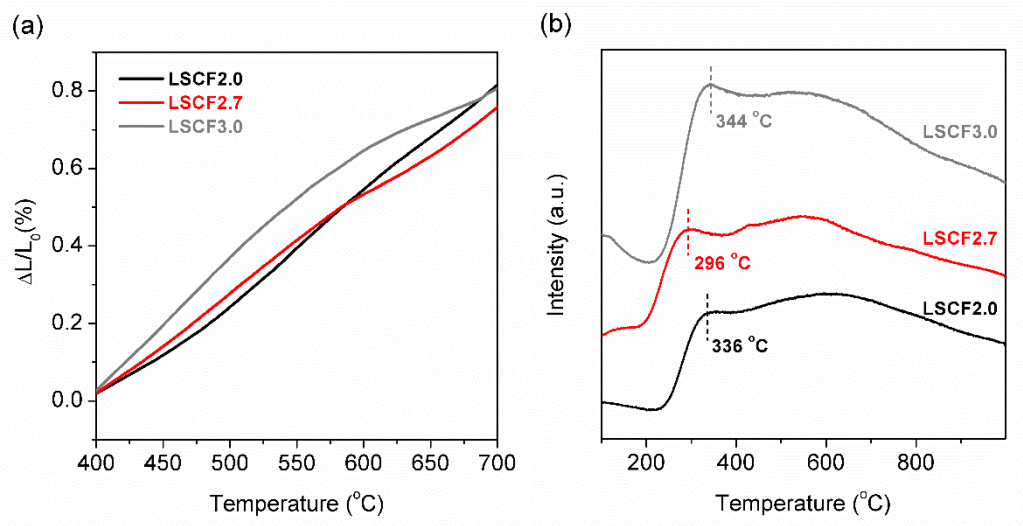

Figure 2. (a) Thermal expansion and (b) O_2-TPD curves for LSCF2.0, LSCF2.7, and LSCF3.0.

The electrical conductivity is one of key indicators for evaluating cathode materials. As shown in **Figure 3**, the conductivity of all LSCFx samples decreases with increasing temperature, indicating their metallic conducting behavior. LSCF2.0 presents the highest electrical conductivity within the whole investigated temperature range. For the RP-SP nanocomposites (LSCF2.5, LSCF2.6, LSCF2.7, and LSCF2.8), the higher the SP phase content (the smaller x value in LSCFx), the higher the apparent conductivity. This is well understood considering the higher conductivity of SP LSCF2.0 than that of RP LSCF3.0. Nevertheless, all samples still show the electrical conductivity of larger than 140 S cm^{-1} within the ILT range of 400-650 °C, which is sufficient to meet the requirements as the cathodes of ILT-SOFCs.

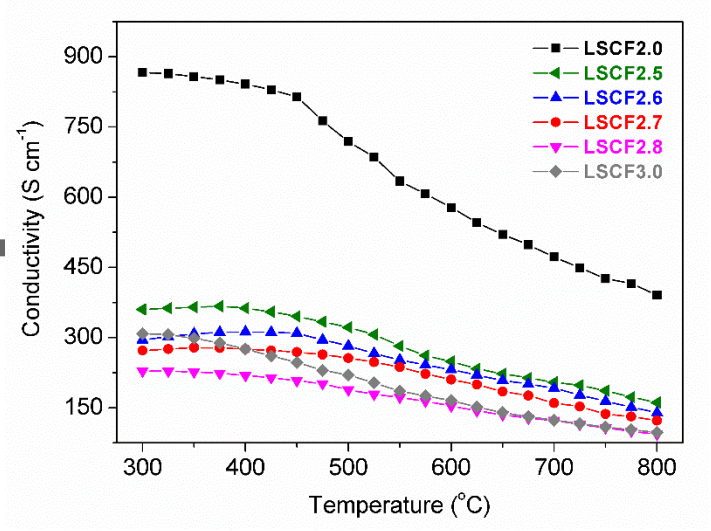

Figure 3. The temperature dependence of the electrical conductivities of LSCFx (x = 2.0, 2.5, 2.6, 2.7, 2.8, and 3.0).

2.2. Electrode Activity

As mentioned above, the cathodic reactions in PCFCs include the electrochemical reduction of molecular oxygen to oxygen ions, and the formation of water from oxygen ions and proton transported from the anode side. For a proton-insulated electrode, the water formation only occurs at the triple-phase-boundary (TPB) of electrode, air and electrolyte, while it can extend to the entire cathode surface if proton conduction is introduced into the cathode bulk. However, in O-SOFCs, only ORR occurs in the cathode, while the water is produced in the anode. It suggests that both the catalytic activity for ORR and the proton conductivity of the electrode determine the cathode

performance in PCFCs. The poor proton conductivity of the cathode may cause a large polarization resistance for the proton charge transfer across the electrolyte-electrode interface. Therefore, the key step to optimize the cathode performance in PCFCs is the introduction of sufficient proton conductivity into the cathode.

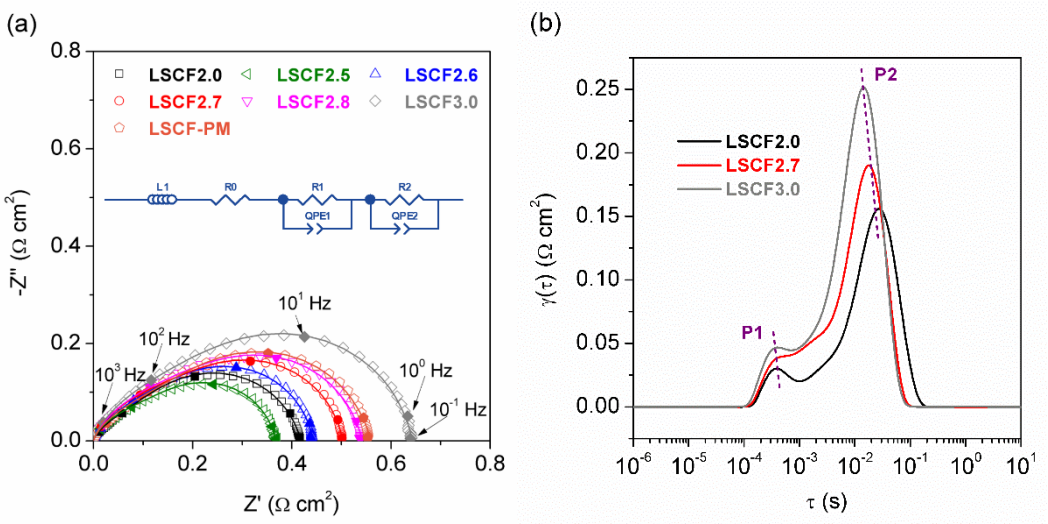

Figure 4. (a) Nyquist plots of LSCFx and LSCF-PM electrodes, and (b) DRT spectra of LSCFx electrodes on the SDC electrolyte at 600 °C in humidified air.

To understand the effect of phase and composition on the catalytic activity for ORR, we first tested the electrochemical performance of the LSCFx materials on oxygen ion-conducting electrolyte (SDC) using a symmetrical cell configuration. **Figure 4**a shows the experimental and fitting results in Nyquist plots of the LSCFx electrodes on the SDC electrolyte in air at 600 °C, where suppressed and

strongly overlapped semicircles appear. For comparison, we physically mixed LSCF2.0 and LSCF3.0 with a mass ratio of 3:7 based on the XRD analysis result of LSCF2.7 to form a mixture of RP+SP, named LSCF-PM. Fitting parameters for LSCF2.0, LSCF3.0 and LSCF2.7 electrodes are listed in Table S1. Typically, the semicircle at different frequencies is related to different processes, including the gas diffusion and surface adsorption (low frequency), the surface diffusion and oxygen dissociation (intermediate frequency), and the charge transfer process (high frequency). All electrodes have no such arcs at low frequencies, which indicates that the polarization resistance from gas diffusion and surface adsorption processes is negligible. The arc at the high frequency range is smaller than that at the intermediate frequency range, suggesting that the polarization resistance of the LSCF series electrodes on the SDC electrolyte mainly arises from the oxygen surface diffusion and oxygen dissociation processes. As shown in Figure 4a, the electrochemical impedance spectroscopy (EIS) of all electrodes displayed similar shapes, manifesting their similar mechanisms for ORR on the oxygen ion-conducting electrolyte. This is also supported by the similar activation energies (E_a) for area specific resistances (ASRs) as shown in Fig. S2, i.e., the E_a values are 118, 131, 126, 123, 123, 124, and 120 kJ mol^{-1} for LSCF2.0, LSCF2.5, LSCF2.6, LSCF2.7, LSCF2.8, LSCF3.0, and LSCF-PM, respectively. From Figure S3, we also find that the LSCF3.0 with a RP structure has the largest ASR, while the LSCF2.0 SP shows much lower ASR. For example, the ASRs are 0.65 and 0.42 Ω cm^2 for LSCF3.0 and LSCF2.0 at 600 °C, respectively. It suggests that LSCF on the SDC electrolyte, the formation of the RP structure can cause a decreased oxygen reaction kinetics compared to the SP structure. After the

creation of RP-SP nanocomposites, the ORR activity is highly dependent on the relative content of the RP and SP phases. For instance, ASRs of 0.37, 0.44, 0.51, and 0.55 Ω cm^2 were observed for the LSCF2.5, LSCF2.6, LSCF2.7, and LSCF2.8, respectively. The larger the SP phase content in the nanocomposite, the smaller the ASR. Interestingly, the LSCF2.5 even showed a smaller ASR (0.37 Ω cm^2) than SP LSCF2.0 (0.42 Ω cm^2). This is possibly because the strongly interacted RP and SP phases leads to an enhanced oxygen mobility in the nanocomposite (Figure 2b), which effectively improves the oxygen reduction kinetics on the electrode surface.

We further performed distribution of relaxation times (DRT) analysis on EIS,[55] and the results are shown in Figure 4b and Figure S4. For all samples, two peaks appeared on DRT curves within the τ ranges of 10^{-3}-10^{-4} s (P1) and 10^{-1}-10^{-3} s (P2). The P1 is assigned to the charge transfer associated with the incorporation of formed O^{2-} into the surface oxygen vacancies, while the P2 is related to the surface oxygen diffusion and dissociation processes. It clearly shows that the intensity of P2 is much higher than that of P1, which further confirms that the polarization resistance of the LSCFx electrode on the SDC electrolyte is mainly contributed by the oxygen surface diffusion and dissociation processes.

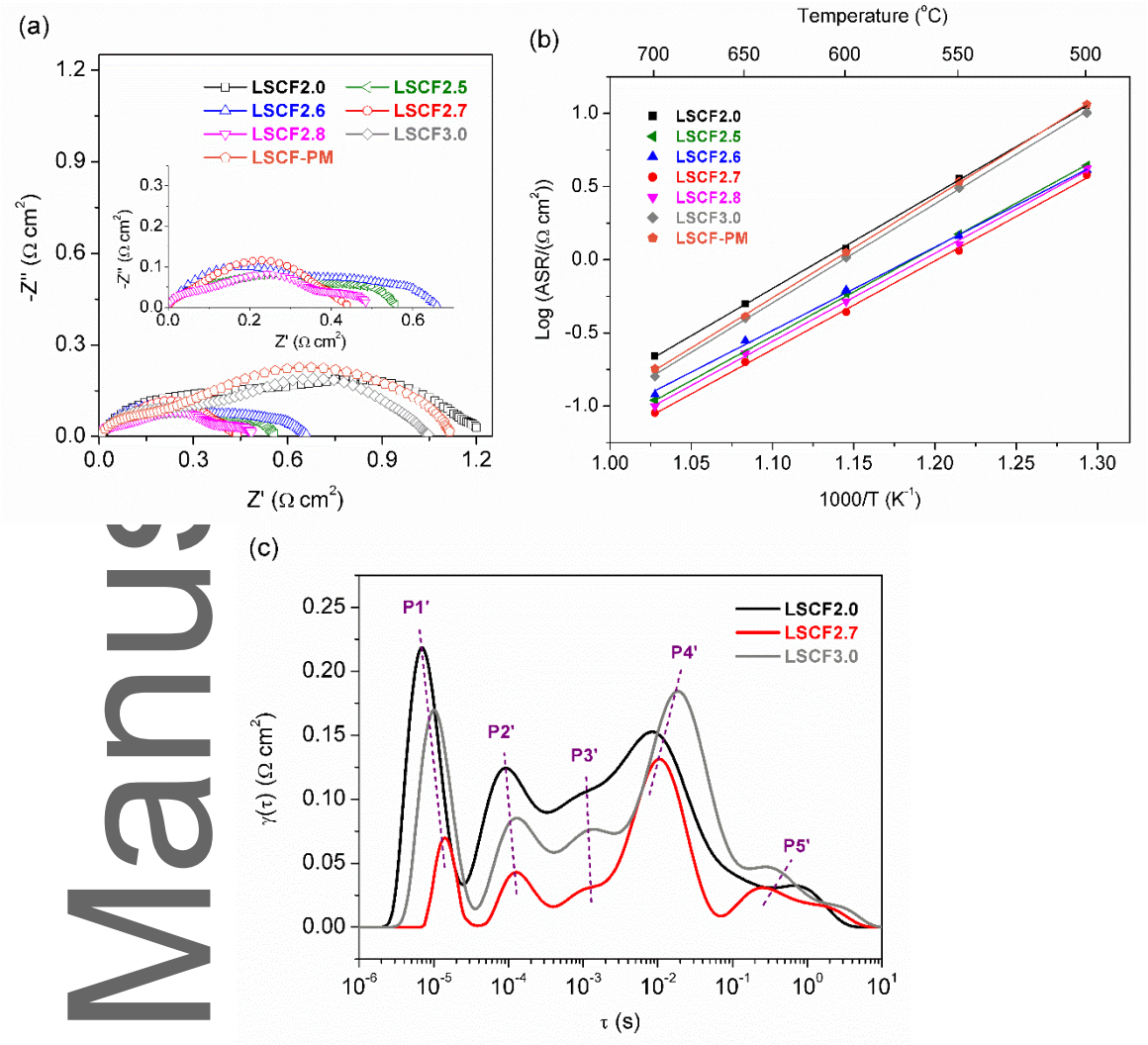

Figure 5. (a) Nyquist plots and (b) temperature dependence of ASRs of LSCFx and LSCF-PM electrodes on the BZCY172 electrolyte at 600 °C in humidified air. (c) DRT spectra of LSCFx electrodes on the BZCY172 at 600 °C.

By applying the LSCFx electrodes on the proton-conducting electrolyte (BZCY172), it can be observed that the EIS trend of the electrodes is different from that on the SDC electrolyte, as shown in **Figure 5**a. Both LSCF2.0 and LSCF3.0 showed relatively poor electrode performance. In fact, at the entire investigated temperature range of 500-700 °C, the SP LSCF2.0 presented the largest ASRs, while the RP LSCF3.0 showed only slightly better performance than LSCF2.0 (Figure 5b). It is well known that the LSCF2.0 has negligible proton conductivity, which may account for its poor electrode performance on the BZCY172 electrolyte. According to density functional theory calculations and experimental studies, it is believed that the formation of RP structure can improve the proton conductivity, which mainly appears in the alkaline earth metal oxide layer.[56-58] However, the LSCF3.0 electrode displayed an unfavorable performance on the BZCY172 electrolyte, which may be explained by the relatively poor ORR activity of LSCF3.0, as evidenced by the EIS results on the SDC electrolyte. Most notably, once RP-SP nanocomposites were formed, their electrode performance on the BZCY172 electrolyte has been substantially improved. Among all nanocomposites, LSCF2.7 delivered the best performance with an ASR of only 0.44 Ω cm^2 at 600 °C, while the ASRs of LSCF2.0 and LSCF3.0 were 1.20 and 1.04 Ω cm^2 at the same temperature, respectively. As demonstrated earlier, on the oxygen-ion conducting electrolyte (SDC), the ORR activity of the nanocomposites was better than RP LSCF3.0 and comparable to SP LSCF2.0. The performance of the LSCFx electrodes on the proton-conducting electrolyte was greatly improved, revealing that the creation of RP-SP

nanocomposites may also bring about a significant increase in proton conductivity compared with SP LSCF2.0.

To support this assumption, the EIS of various LSCFx electrodes on the BZCY172 electrolyte was also analyzed by DRT, which can provide more in-depth information on the contribution of different parts of the electrode reactions to the polarization resistance, as shown in Figure 5c and Figure S5. As mentioned, on the SDC electrolyte, all the samples showed two peaks, assigning to the incorporation of O^{2-} into surface oxygen vacancy and the oxygen surface diffusion/dissociation, respectively. The DRT curves of the LSCFx electrodes on the BZCY172 electrolyte are much more complicated than that on the SDC electrolyte. The main difference is the appearance of a strong peak (P1') at the τ range of 10^{-5}-10^{-6} s. Such peak in high frequency should be related to charge transfer process as well. In combination with the literature results, it is assigned to the proton transfer across the electrolyte-electrode interface.[60,61] As shown in Figure 5c, LSCF2.0 SP showed the largest intensity for P1'. This is easy to understand since LSCF2.0 is a proton-insulating material, and the proton charge transfer only occurs at the TPB. Compared to LSCF2.0, LSCF3.0 showed a lower intensity of P1', suggesting an increase in proton conductivity. It agrees well with the easier proton conduction in RP than in SP. Surprisingly, for all RP-SP nanocomposites, the intensity of P1' was extremely decreased, indicating the substantial increase of proton conductivity within the nanocomposite electrodes, which further confirms the creation of synergy between the SP and RP phases in the nanocomposites. The proton conduction in perovskite oxides is mainly through

hydroxide defects that can be generated by the dissociative adsorption of water in oxygen vacancies.[59] The peak (P2') within the τ range of 10^{-3}-10^{-4} s was also observed in the DRT curves for the LSCFx electrodes on the BZCY172 electrolyte, while its intensity was slightly increased compared with that on the SDC electrolyte. As we all know, the air used in PCFCs is humidified, and the water in the air will be competitively adsorbed in the oxygen vacancies of the electrode, thus inhibiting the charge transfer of oxygen ions. Nevertheless, the intensity of P2' is still much lower than that of P1'. Therefore, the charge transfer of oxygen ions will have a decisive effect on electrode performance. Another difference is that, in some cases, an obvious gas diffusion polarization peak (P3') was observed in the DRT curve of the LSCF2.7 electrode on the BZCY172 electrolyte, but this peak did not appear for the same electrode on the SDC electrolyte. Similarly, the water in the humidified air probably hindered the oxygen diffusion under the operating conditions of PCFCs. Owing to the low intensity of P3', such gas phase diffusion polarization also did not play pivotal role in electrode performance. Although the peak shape became less symmetrical compared to that on the SDC electrolyte, obvious peaks at the intermediate frequency range (τ = 10^{-1}-10^{-3} s) were observed for the DRT curves of the LSCFx on the BZCY172 electrolyte, and the intensity of the peak is comparable to that on the SDC electrolyte. Undoubtedly, this peak is related to the oxygen surface diffusion and dissociation processes. On the basis of the DRT analysis, it is clear that the electrode performance on the proton-conducting electrolyte mainly depends on the ORR activity and the proton conductivity of the electrode. The electrode performance of the LSCFx nanocomposites is better than LSCF2.0

and LSCF3.0, which is mainly due to the increase of the proton conductivity inside the electrode bulk.

For comparison, we also analyzed the EIS of the LSCF-PM electrode on the BZCY172 electrolyte in the humidified air (Figure 5a and 5b). Compared to LSCF2.0 and LSCF3.0 electrodes, the LSCF-PM electrode showed moderately improved activity. For example, their ASRs are 1.20, 1.04, and 1.11 Ω cm^2 for LSCF2.0, LSCF3.0, and LSCF-PM at 600 °C, respectively. The enhancement is much less obvious in comparison to the LSCF2.7 electrode. As we are aware, before physically mixing LSCF2.0 and LSCF3.0, although they are nanocrystallines, they have aggregated into micro-sized grains due to the high-temperature sintering process. This is supported by the large intensity of P1' in the DRT curve of the LSCF-PM electrode on the BZCY172 electrolyte (Figure S5). It signifies that the creation of strongly interacted nanocomposites with abundant RP-SP interface is essential to increase the proton conductivity, so as to boost the electrode performance. Nonetheless, more in-depth investigation is needed to understand the mechanism of such improvement.

2.3. Cell Performance

The superior electrochemical performance of the RP-SP nanocomposite as the cathode of PCFC was further verified by the single cell performance test. **Figure 6**a compares the *I-V* and *I-P* polarization curves of three anode-supported single PCFCs with three different cathodes, i.e., LSCF2.0, LSCF3.0, and LSCF2.7. To ensure any difference in cell performance mainly originates from

the cathode of fuel cells, we adopted the same fabrication technique and parameters for these three cells, and the electrolyte thickness was found to be approximately 28 μm. As expected, the PCFC with the LSCF2.7 cathode delivered the highest power outputs within the investigated temperature range (500-700 °C), such as the peak power densities (PPDs) of 276, 289, and 391 mW cm^{-2} were achieved at 600 °C for the fuel cells with LSCF2.0, LSCF3.0, and LSCF2.7 cathodes, respectively. Figure 6b shows the EIS of these three cells

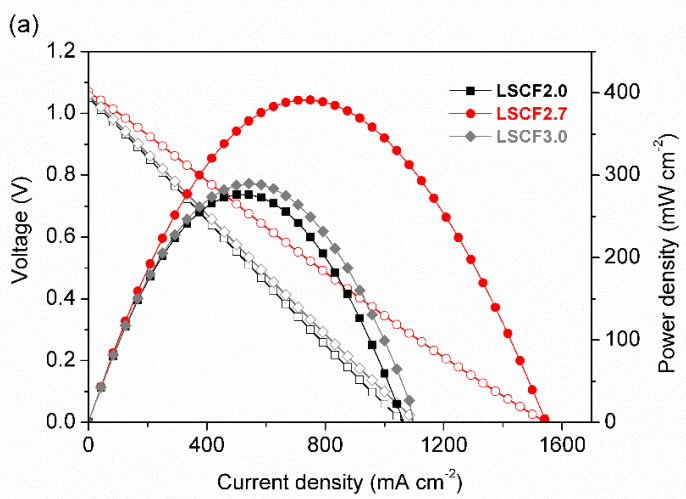

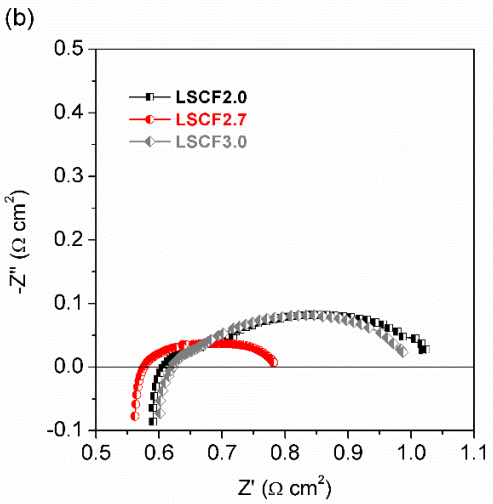

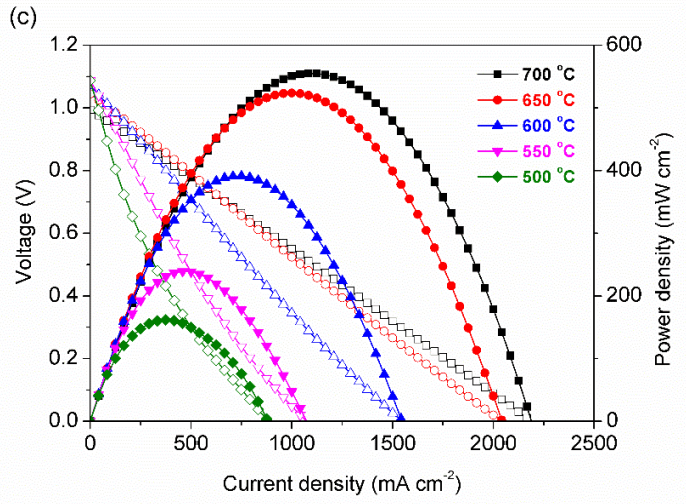

Author

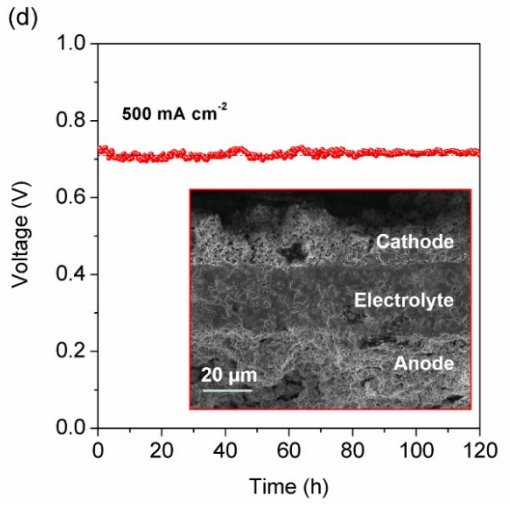

Figure 6. (a) The *I-V-P* curves and (b) EIS of PCFCs with different cathodes at 600 °C, (c) the *I-V-P* curves and (d) stability of the PCFC with LSCF2.7 cathode at 600 °C. The inset in Figure 6d is the SEM image of the PCFC after the stability test.

under open-circuit voltage (OCV) conditions. The PCFC with the LSCF2.7 cathode demonstrated the smallest total electrode polarization resistance. As noted above, these fuel cells we tested have the same anode and electrolyte composition and thickness, so the performance difference is principally attributed to the cathode activity. In other words, the LSCF2.7 had the smallest cathodic polarization resistance. Combined with the DRT analysis above, the improved performance is largely due to the introductionof proton conduction into the cathode of PCFC. Recently, many cathodes with triple-conducting ($e^-/O^{2-}/H^+$) have been developed for PCFCs and proved to have excellent activity,[9,59,62] because the reactive sites of such cathodes extend to the entire cathode surface. As shown in Figure 6c, the PCFC with the LSCF2.7 cathode generated favorable PPDs of 555, 524, 391, 239, and 162 mW

cm^{-2} at 700, 650, 600, 550, and 500 °C, respectively. The power outputs are comparable to that of PCFCs with many well-known high-performance cathodes reported in the literature, especially at temperatures below 600 °C.[11-13,17,18] The polarization resistances of this PCFC were 0.05, 0.08, 0.21, 0.56, and 2.2 Ω cm^2 at 700, 650, 600, 550, and 500 °C, respectively (Figure S6), which are slightly lower than that tested with symmetrical cells at the corresponding temperatures.

Besides the catalytic activity, durability is another important indicator to evaluate a cathode material. Phase transition, interface reaction between different cell components, surface poisoning, and electrode sintering could all give rise to a degradation of electrode performance. The operational stability of the LSCF2.7 cathode was investigated on the basis of cell performance at a constant polarization current of 500 mA cm^{-2}. As shown in Figure 6d, no significant performance degradation was observed during the 120-hour test period, indicating the favorable durability of the LSCF2.7 cathode under the practical operating conditions of PCFCs. Moreover, from the scanning electron microscope (SEM) image of the cross-section of the PCFC after the stability test (the inset in Figure 6d), the LSCF2.7 cathode was still firmly adhered to the electrolyte layer without any delamination. It suggests that LSCF2.7 has excellent thermomechanical compatibility with the proton-conducting electrolyte (BZCY172). The strong interaction between the RP and SP phases in the nanocomposite effectively suppresses thermal expansion of the material, which may contribute to the favorable thermomechanical compatibility of the LSCF2.7 electrode and the BZCY172 electrolyte. As demonstrated above, the LSCF2.7 has good structural stability under operating

conditions (Figure 1a). The combination of high structural stability and robust thermomechanical stability then contributed to the satisfactory operational stability of the LSCF2.7 cathode in a single PCFC.

3. Conclusion

In summary, the new family of RP-SP nanocomposites, LSCFx (x=2.5, 2.6, 2.7 and 2.8), have been successfully developed as the potential efficient cathodes for PCFCs. After the formation of the RP-SP nanocomposites, the ORR activity over the proton-conducting electrolyte was enhanced. The charge transfer between the cathode and the electrolyte was improved owing to the proton conductivity of the RP-SP nanocomposites. The PCFC using LSCF2.7 as the cathode exhibited the best electrochemical performance, with a PPD of 391 mW cm^{-2} and a polarization resistance of 0.21 Ω cm^2 at 600 °C. These findings highlight the potential application of RP-SP composites as highly active and durable electrodes for PCFCs, which may greatly stimulate the development of PCFCs.

4. Experimental Section

Materials Synthesis: LSCFx cathode and BZCY172 proton-conducting electrolyte materials were synthesized by a facile one-pot sol-gel method. Metal nitrates as the raw materials of cation sources in oxides were first dissolved in water, and then the complexing agents,

ethylenediaminetetraacetic acid (EDTA) and citric acid (CA), were added at a molar ratio of 1 : 1 : 2 (total metal cations : EDTA : CA). The pH value of above solution was adjusted to around 7 using ammonia solution. When the solution became a clear gel, it was preheated at 250 °C for at least 5 h. After that, the precursor was further calcined in air at 1100 °C for 5 h to produce the oxide with the thermodynamically stable phase structure. The SDC oxygen-ion conducting electrolyte material was purchased from fuelcellmaterials (USA). The anode powders were prepared by ball-milling 3.5 g of electrolyte material, 6.5 g of NiO, 0.3 g of polyvinyl butyral (PVB), and 0.5 g of starch in the ethanol for 30 min, and then the anode slurry was dried and ground for the subsequent use.

Cell Fabrication: Symmetrical cells were adopted for evaluating the electrochemical performance of cathode materials. First, dense electrolyte (SDC and BZCY172) discs with the thickness of ~0.5 mm and the diameter of 15 mm were fabricated by dry-pressing and sintering in air at 1400 °C for 5 h. After sintering, the diameter of electrolyte discs was shrunk to ~12.5 mm. The cathode slurry was prepared by ball-milling the cathode powders in a mixed solution of isopropanol, ethylene glycol, and glycerol, and painted on both sides of the electrolyte discs. Then, the symmetrical cells were calcined in the air at 1000 °C for 2 h. Anode-supported SOFCs with thin-film electrolyte were used for cell performance test. 0.35 g of anode powder was first dry-pressed into a disc, and then 0.02 g of electrolyte power was distributed homogeneously on the surface of the anode disc. The obtained anode-electrolyte dual layer cells were co-sintered in air at 1400 °C for 5 h to allow the densification of the electrolyte layer. The cathode slurry was finally coated in the middle

of the electrolyte surface with an effective area of 0.48 cm^2, and then sintered in air at 1000 °C for 2 h. Silver and ceramic pastes were used as the current collector and the sealant, respectively.

Characterizations and Electrochemical Performance Measurement: The phase structure of the as-synthesized oxides were confirmed by the XRD (Bruker D8 Advance) with filtered Cu-Kα radiation. N_2 adsorption/desorption isotherms were collected on a Micromeritics TriStar II instrument, and the specific surface areas of oxides were attained using Barrett-Emmett-Teller (BET) model. The TECs of materials were determined using a Netzsch DIL 402C/3/G dilatometer from 200 to 800 °C with an air-purge flow rate of 50 mL min^{-1} [STP]. The morphology of the SOFC was observed using a Zeiss 1555 field-emission variable-pressure scanning electron microscope. The oxygen desorption ability of the materials was studied using O_2–TPD technique.[63] The electrical conductivity was measured by a 4-probe DC method as reported in our previous publications.[63] For the symmetrical cell test, air passing through water at room temperature was introduced to the cathode. The EIS was conducted using Solartron 1260 frequency response analyzer combined with Solartron 1287 potentiostat. The measurement frequency was 10^{-1} to 10^6 Hz. For the cell performance test, the cathode was exposed to ambient air, while hydrogen passing through water at room temperature was introduced to the anode. The gas flow rate was 60 mL min^{-1}. The *I-V* and *I-P* polarization curves of fuel cells were collected by a Keithley 2440 sourcemeter.

Supporting Information

Supporting Information is available from the Wiley Online Library or from the author.

Acknowledgements

This work was supported from Australian Research Council (ARC) Discovery Project Grant DP200103315. Dr. Chao Su would like to thank the ARC Discovery Early Career Researcher Award DE180100773.

Received: ((will be filled in by the editorial staff))
Revised: ((will be filled in by the editorial staff))
Published online: ((will be filled in by the editorial staff))

References

[1] Y. Liu, Z. Shao, T. Mori, S. P. Jiang, *Mater. Rep. Energy* **2021**, *1*, 100003.

[2] Z. Lyu, Y. Wang, Y. Zhang, M. Han, *Chem. Eng. J.* **2020**, *393*, 124755.

[3] H. Shi, Q. Li, W. Tan, H. Qiu, C. Su, *Chin. J. Chem. Eng.* **2020**, *28*, 1156.

[4] Y. Zhang, B. Chen, D. Guan, M Xu, R. Ran, M. Ni, W. Zhou, R. O'Hayre, Z. Shao, *Nature* **2021**, *591*, 246.

[5] M. Ni, Z. Shao, *Science* **2020**, *369*, 138.

[6] H. Shi, C. Su, R. Ran, J. Cao, Z. Shao, *Prog. Nat. Sci.* **2020**, *30*, 764.

[7] D. Han, X. Liu, T. S. Bjørheim, T. Uda, *Adv. Energy. Mater.* **2021**, *11*, 2003149.

[8] W. Wang, D. Medvedev, Z. Shao, *Adv. Funct. Mater.* **2018**, *28*, 1802592.

[9] C. Duan, J. Tong, M. Shang, S. Nikodemski, M. Sanders, S. Ricote, A. Almansoori, R. O'Hayre, *Science* **2015**, *349*, 1321.

[10] C. Zhou, J. Sunarso, Y. Song, J. Dai, J. Zhang, B. Gu, W. Zhou, Z. Shao, *J. Mater. Chem. A* **2019**, *7*, 13265.

[11] J. Xiao, L. Chen, H. Yuan, L. Ji, C. Xiong, J. Ma, X. Zhu, *Mater. Lett.* **2017**, *189*, 192.

[12] K. Lee, C. Tseng, S. Jang, J. Lin, K. Wang, J. Chang, T. Chen, S. Lee, *Int. J. Hydrogen Energy*, **2019**, *44*, 23784.

[13] J. Chen, J. Li, L. Jia, I. Moussa, B. Chi, J. Pu, J. Li, *J. Power Sources* **2019**, *428*, 13.

[14] J. Li, C. Wang, X. Wang, L. Bi, *Electrochem. Commun.* **2020**, *112*, 106672.

[15] Y. Chen, S. Yoo, K. Pei, D. Chen, L. Zhang, B. deGlee, R. Murphy, B. Zhao, Y. Zhang, Y. Chen, M. Liu, *Adv. Funct. Mater.* **2018**, *28*, 1704907.

[16] F. He, M. Liang, W. Wang, R. Ran, G. Yang, W. Zhou, Z. Shao, *Energy Fuels* **2020**, *34*, 11464.

[17] H. Lv, Z. Jin, R. Peng, W. Liu, Z. Gong, *Ceram. Int.* **2019**, *45*, 23948.

[18] B. Liu, L. Jia, B. Chi, J. Pu, J. Li, *Compos. B. Eng.* **2020**, *191*, 107936.

[19] R. Zohourian, R. Merkle, G. Raimondi, J. Maier, *Adv. Funct. Mater.* **2018**, *28*, 1801241.

[20] Y. Bu, S. Joo, Y. Zhang, Y. Wang, D. Meng, X. Ge, G. Kim, *J. Power Sources* **2020**, *451*, 227812.

[21] R. Ren, Z. Wang, X. Meng, C. Xu, J Qiao, W. Sun, K. Sun, *ACS Appl. Mater. Interfaces* **2020**, *12*, 23959.

[22] G. Yang, C. Su, H. Shi, Y. Zhu, Y. Song, W. Zhou, Z. Shao, *Energy Fuels* **2020**, *34*, 15169.

[23] R. Peng, T. Wu, W. Liu, X. Liu, G. Meng, *J. Mater. Chem.* **2010**, *20*, 6218.

[24] L. Miao, J. Hou, Z. Gong, Z. Jin, W. Liu, *Int. J. Hydrogen Energy* **2019**, *44*, 7531.

[25] Y. G. Lyagaeva, N. A. Danilov, M. Y. Gorshkov, G. K. Vdovin, B. D. Antonov, A. K. Demin, D. A. Medvedev, *Russ. J. Appl. Chem.* **2018**, *91*, 583.

[26] A. Afif, N. Radenahmad, C. M. Lim, M. I. Petra, M. A. Islam, S. M. H. Rahman, S. Eriksson, A. K. Azad, *Int. J. Hydrogen Energy* **2016**, *41*, 11823.

[27] C. Xia, W. Rauch, F. Chen, M. Liu, *Solid State Ionics* **2002**, *149*, 11.

[28] Z. Shao, S. Haile, *Nature* **2004**, *431*, 170.

[29] Y. Zhu, J. Sunarso, W. Zhou, S. Jiang, Z. Shao, *J. Mater. Chem. A* **2014**, *2*, 15454.

[30] S. Mulmi, V. Thangadurai, *Chem. Comm.* **2019**, *55*, 3713.

[31] D. Xie, A. Ling, D. Yan, L. Jia, B. Chi, J. Pu, J. Li, *Electrochim. Acta* **2020**, *344*, 136143.

[32] J. Liu, Z. Jin, L. Miao, J. Ding, H. Tang, Z. Gong, R. Peng, W. Liu, *Int. J. Hydrogen Energy* **2019**, *44*, 11079.

[33] X. Xu, J. Zhao, M. Li, L. Zhuang, J. Zhang, S. Aruliah, F. Liang, H. Wang, Z. Zhu, *Compos. B. Eng.* **2019**, *178*, 107491.

[34] L. Yang, Z. Liu, S. Wang, Y. Choi, C. Zuo, M. Liu, *J. Power Sources* **2010**, *195*, 471.

[35] H. Shimada, Y. Yamaguchi, H. Sumi, Y. Mizutani, *J. Electrochem. Soc.* **2020**, *167*, 124506.

[36] Z. Wang, W. Yang, S. Shafi, L. Bi, Z. Wang, R. Peng, C. Xia, W. Liu, Y. Lu, *J. Mater. Chem. A* **2015**, *3*, 8405.

[37] D. Huan, N. Shi, L. Zhang, W. Tan, Y. Xie, W. Wang, C. Xia, R. Peng, Y. Lu, *ACS Appl. Mater. Interfaces* **2018**, *10*, 1761.

[38] D. Huan, L. Zhang, X. Li, Y. Xie, N. Shi, S. Xue, C. Xia, R. Peng, Y. Lu, *ChemSusChem* **2020**, *13*, 4994.

[39] Y. Chen, B. Qian, G. Yang, D. Chen, Z. Shao, *J. Mater. Chem. A* **2015**, *3*, 6501.

[40] X. Xu, Y. Pan, Y. Zhong, R. Ran, Z. Shao, *Mater. Horiz.* **2020**, *7*, 2519.

[41] A. Khan, H. Wang, Y. Liu, A. Jawad, J. Ifthikar, Z. Liao, T. Wang, Z. Chen, *J. Mater. Chem. A* **2018**, *6*, 1590.

[42] K. Lin, B. Chen, *Chemosphere* **2017**, *166*, 146.

[43] F. Li, Y. Xu, F. Cheng, Y. Yan, S. Xia, J. Liu, L. Jiang, *Ceram. Int.* **2020**, *46*, 6191.

[44] Y. Zhu, Q. Lin, Z. Hu, Y. Chen, Y. Yin, H. Tahini, H. Lin, C. Chen, X. Zhang, Z. Shao, H. Wang, *Small* **2020**, *16*, 2001024.

[45] J. F. Shin, W. Xu, M. Zanella, K. Dawson, S. N. Savvin, J. B. Claridge, M. J. Rosseinsky, *Nat. Energy* **2017**, *2*, 16214.

[46] Y. Chen, J. Shen, G. Yang, W. Zhou, Z. Shao, *J. Mater. Chem. A* **2017**, *5*, 24842.

[47] C. Jin, Y. Mao, D. W. Rooney, W. Sun, N. Zhang, K. Sun, *Int. J. Hydrogen Energy* **2016**, *41*, 4005.

[48] F. Li, L. Jiang, R. Zeng, T. Wei, F. Wang, Y. Xu, Y. Huang, *Int. J. Hydrogen Energy* **2015**, *40*, 12750.

[49] Z. C. Torunoğlu, D. Sarı, O. Demircan, Y. E. Kalay, T. Öztürk, Y. Kuru, *Int. J. Hydrogen Energy* **2018**, *43*, 18642.

[50] J. Hou, Q. Wang, J. Li, Y. Lu, L. Wang, X. Fu, J. Luo, *J. Power Sources* **2020**, *466*, 228240.

[51] X. Xu, Y. Pan, L. Ge, Y. Chen, X. Mao, D. Guan, M. Li, Y. Zhong, Z. Hu, V. K. Peterson, M. Saunders, C. Chen, H. Zhang, R. Ran, A. Du, H. Wang, S. P. Jiang, W. Zhou, Z. Shao, *Small*, **2021**, DOI: 10.1002/smll.202101573.

[52] Y. Zheng, S. He, L. Ge, M. Zhou, H. Chen, L. Guo, *Int. J. Hydrogen Energy* **2011**, *36*, 5128.

[53] Z. Zhu, J. Qian, Z. Wang, J. Dang, W. Liu, *J. Alloys. Compd.* **2013**, *581*, 832.

[54] W. Zhou, R. Ran, Z. Shao, N. Xu, *J. Power Sources*, 2008, *182*, 24.

[55] T. Wan, M. Saccoccio, C. Chen, F. Ciucci, *Electrochim. Acta* **2015**, *184*, 483.

[56] W. Li, B. Guan, L. Ma, S. Hu, N. Zhang, X. Liu, *J. Mater. Chem. A* **2018**, *6*, 18057.

[57] L. Zhang, F. Yao, J. Meng, W. Zhang, H. Wang, X. Liu, J. Meng, H. Zhang, *J. Mater. Chem. A* **2019**, *7*, 18558.

[58] M. Chen, Y. Xuan, F. Zhang, L. He, X. Wang, H. Pan, J. Ren, Z. Lin, *Int. J. Hydrogen Energy* **2020**, *45*, 14964.

[59] R. Ren, Z. Wang, C. Xu, W. Sun, J. Qiao, D. W. Rooney, K. Sun, *J. Mater. Chem. A*, **2019**, *7*, 18365.

[60] A. Tarutin, J. Lyagaeva, A. Farlenkov, S. Plaksin, G. Vdovin, A. Demin, D. Medvedev, *Mater.* **2019**, *12*, 118.

[61] D. Lim, H. Im, B. Singh, S. Song, *J. Electrochem. Soc.* **2015**, *162*, F547.

[62] Y. Song, Y. Chen, W. Wang, C. Zhou, Y. Zhong, G. Yang, W. Zhou, M. Liu, Z. Shao, *Joule*, **2019**, *3*, 2842.

[63] R. Ran, Y. Guo, D. Gao, S. Liu, Z. Shao, *Sep. Purif. Technol.* **2011**, *81*, 384.

[1] Ruddlesden-Popper and single perovskite nanocomposites (RP-SP) are synthesized by a facile one-pot method. Due to the synergistic effect between the RP and SP phases, the obtained nanocomposite possesses enhanced proton-conductivity. Therefore, compared with pure RP and SP cathodes, the protonic ceramic fuel cell with this new nanocomposite cathode delivers the best cell performance.

[2] Huangang Shi, Chao Su,* Xiaomin Xu, Yangli Pan, Guangming Yang, Ran Ran, and Zongping Shao*

[3]

[4] **Building Ruddlesden-Popper and Single Perovskite Nanocomposites: A New Strategy to Develop High-Performance Cathode for Protonic Ceramic Fuel Cells**

[5]